PAPER • **OPEN ACCESS**

Pure spin current injection of single-layer monochalcogenides

To cite this article: Bernardo S Mendoza *et al* 2023 *Mater. Res. Express* **10** 035003

Materials Research Express

OPEN ACCESS

RECEIVED
4 November 2022

REVISED
13 February 2023

ACCEPTED FOR PUBLICATION
27 February 2023

PUBLISHED
7 March 2023

PAPER

Pure spin current injection of single-layer monochalcogenides

Bernardo S Mendoza[1,*], **Simone Grillo**[2], **Lucila Juárez-Reyes**[1] **and Benjamin M Fregoso**[3]

[1] Centro de Investigaciones en Óptica, A.C., León, Guanajuato, 37150, Mexico
[2] University of Rome 'Tor Vergata' and INFN, Via della Ricerca Scientifica 1, 00133, Rome, Italy
[3] Department of Physics, Kent State University, Kent, OH 44242, United States of America
[*] Author to whom any correspondence should be addressed.

E-mail: bms@cio.mx

Keywords: spin current, 2D-monochalcogenides, *ab-initio*

Abstract

We compute the spectrum of pure spin current injection in ferroelectric single-layer SnS, SnSe, GeS, and GeSe. The formalism takes into account the coherent spin dynamics of optically excited conduction states split in energy by spin–orbit coupling. The velocity of the electron's spins is calculated as a function of incoming photon energy and angle of linearly polarized light within a full electronic band structure scheme using density functional theory. We find peak speeds of 520, 360, 270 and 370 Km s^{-1} for SnS, SnSe, GeS and GeSe, respectively which are an order of magnitude larger than those found in bulk semiconductors, e.g., GaAs and CdSe. Interestingly, the spin velocity is almost independent of the direction of polarization of light in a range of photon energies. Our results demonstrate that single-layer SnS, SnSe, GeS and GeSe are candidates to produce on demand spin-current in spintronics applications.

1. Introduction

There is increasing interest in attaining precise control of the spin of electrons at mesoscopic scales because it could lead to novel quantum computation platforms [1–4] Pure spin current (PSC), i.e., spin current with no associated charge current, could lead to more efficient quantum devices because a PSC does not produce joule heating. A PSC can be realized in the spin Hall effect [5], one photon absorption of light [6–8], or interference of two optical beams [9–11].

In contrast to the well-known spin Hall effect, which is a ground state phenomenon, optically induced PSC occurs in excited states of the material. A simple argument for the existance of PSC is as follows, linearly polarized light injects carriers symmetrically into $\pm\boldsymbol{k}$ conduction states in the Brillouin zone (BZ). Yet, the velocity and spin operators are odd under time reversal symmetry and hence there is no net charge current [6, 12, 13] or spin density after summation over all the BZ [14]. However, the spin current is even under time reversal and hence it does not vanish after summation over all the BZ. The optical PSC will manifests as a spatial separation of spin-up spin-down components or electrons. Optical PSC has been measured by pump-probe techniques in GaAs [15, 16], AlGaAs [16], ZnSe [17] and Co_2FeSi [18].

One of the difficulties in creating measurable spin current and developing of PSC based semiconductor spintronic devices is the fact that the spin relaxation time in conventional semiconducting materials could be too short to enable spin transport, and may result in a nonobservable spin current [19–23].

For this reason we turn our attention to novel two-dimensional (2D) materials. Since the discovery of graphene, two-dimensional materials such as silicene, black phosphorus, hexagonal boron nitride, etc., have been widely investigated. In general, it is interesting to explore the properties of this novel type of materials, for 2D materials represent the ultimate scaling in thickness with mechanical, optical, and electronic properties that are unique relative to their bulk counterparts. Indeed, 2D materials are the next frontier in science and technology in general. Recently, layered bulk materials attracted much interest because their experimentally grown structures show very promising and novel properties. These materials are composed of single-layer units piled and weakly bonded via van der Waals interactions. This fact allows the structure to be exfoliated layer by

layer and reduce, in principle, the dimensionality up to a single layer. Indeed, it has been found that 2D materials exhibit even more interesting properties than their bulk counterpart. From the point of view of potential applications of this new materials in the realization of new optical and electronic devices, in the context of nanostructuring efforts, the main challenges for the scientific community consists on improving the eco-sustainability of the construction processes, finding valid alternatives to materials which are expensive to obtain and dangerous for the people and the environment. In this sense, single-layer or 2D group-IV lead-free monochalcogenides, including GeS, GeSe, SnS, and SnSe have attracted great attention and are actively being investigated [24–34], since these compounds are abundant, non-toxic and can generally be produced with relatively easy procedures [35, 36]. Moreover, due to their very interesting properties such as band gaps and large carrier mobilities, these materials are very promising candidates for optoelectronics applications. However, up to now, concerning spin currents, this class of 2D materials has not been yet investigated. While monochalcogenides are centrosymmetric in the bulk, their 2D counterparts lack inversion symmetry, thus allowing in practice the generation of non-linear effects such as optical PSC. However, in principle one should still be able to show that GeS, GeSe, SnS, and SnSe possess desirable spin relaxation times similar to that of the semiconductors for which PSC has already been measured GaAs [15, 16]. AlGaAs [16], and ZnSe [17].

In this paper we show that 2D ferroelectric GeS, GeSe, SnS, and SnSe exhibit large optical PSC as measured by the spin velocity injection (SVI) to be defined below. We compute the spectrum of SVI as a function of photon energy ($\hbar\omega$) and angle of linearly polarized light. We consider the case of the particles moving on the plane of the slab and spin pointing out of the slab. Monolayer SnS was recently experimentally realized [37], and hence our theoretical results have direct experimental relevance for these materials. Indeed, we find that each structure has as a function of $\hbar\omega$ a rich variety of SVI that reaches values as high as ∼520 Kms^{-1} for SnS, ∼360 Km s^{-1} for SnSe, ∼280 Km s^{-1} for GeS and ∼360 Km s^{-1} for GeSe, and by changing the direction of the linearly polarized electric field that induces SVI, its direction could be controlled, thus giving ample possibilities to manipulate it at will. The large SVI values in turn lead to average distances that separates the up-spins from the down-spins in the PSC, which are ∼20 larger than those of bulk semiconductors where it has been experimentally measured [15–17], giving a larger physical space for applications, like gates that could detect the PSC.

This paper is organized as follows. In section 2, we present the PSC theoretical formalism, showing the main expressions used to numerically implement PSC and SVI calculations. In section 3 we describe the 2D monochalcogenide SnS, SnSe, GeS and GeSe structures and in section 4, we describe numerical method. In section 5 we present and analyze the results corresponding to the SVI spectra for SnS and in appendix A we present the results for SnSe, GeS and GeSe. Finally, we summarize our findings in section 7.

2. Theory

In this section we follow the formalism of [7, 8] and present only the main theoretical results that lead to the calculation of PSC. We consider free electrons characterized by a Bloch Hamiltonian, $\hat{H}$, that includes the Spin-Orbit Coupling (SOC) needed in order to calculate the spin matrix elements of the electrons used for PSC. We have that

$$\hat{H} = \hat{H}_0 + \hat{H}_{\rm SOC}, \tag{1}$$

where

$$\hat{H}_0 = \frac{\hat{p}^2}{2m} + \hat{V}(\boldsymbol{r}), \tag{2}$$

gives the ground state of the system, with m the mass, $\hat{\boldsymbol{r}}$ the position and $\hat{\boldsymbol{p}} = -i\hbar\,\boldsymbol{\nabla}$ the momentum of the electron, and $\hat{V}(\hat{\boldsymbol{r}})$ is the periodic crystal potential. Also,

$$\hat{H}_{\rm SOC} = \gamma\hat{\boldsymbol{S}}\cdot\hat{\boldsymbol{L}}, \tag{3}$$

is the SOC hamiltonian derived from Dirac's equation [38], where $\hat{\boldsymbol{L}} = \hat{\boldsymbol{r}}\times\hat{\boldsymbol{p}}$ and $\hat{\boldsymbol{S}} = (\hbar/2)\hat{\boldsymbol{\sigma}}$, are the angular momentum and the spin of the electron, with $\hat{\boldsymbol{\sigma}}$ the Pauli spin matrices. For the static spherical potentials used in here, $\hat{V}(\boldsymbol{r}) = V(r)$, and $\gamma = (1/2m^2c^2r)dV(r)/dr$.

The solution of equation (1) is written as

$$\hat{H}|n\boldsymbol{k}\rangle = \hbar\omega_n(\boldsymbol{k})|n\boldsymbol{k}\rangle, \tag{4}$$

with $\hbar\omega_n(\boldsymbol{k})$ the energy of the electronic band n at point $\boldsymbol{k}$ in the Irreducible Brillouin Zone (IBZ) and $|n\boldsymbol{k}\rangle$ the Bloch spinor state, given by

$$\langle \boldsymbol{r}|n\boldsymbol{k}\rangle = \begin{pmatrix} \psi^{(1)}_{n\boldsymbol{k}}(\boldsymbol{r}) \\ \psi^{(2)}_{n\boldsymbol{k}}(\boldsymbol{r}) \end{pmatrix}, \tag{5}$$

where $\psi^{(1,2)}_{n\boldsymbol{k}}(\boldsymbol{r})$ are its two components.

The free electrons are subjected to an external homogeneous electric field

$$\boldsymbol{E}(t) = \boldsymbol{E}(\omega)e^{-i\omega t} + c.c., \tag{6}$$

that perturbs the system through the length-gauge Hamiltonian

$$H_p(t) = -er^a E^a(t), \tag{7}$$

where e is the electron charge. The latin superscript indicate Cartesian coordinates and we follow Einstein convention of repeated indices.

We mention that the valence and conduction bands in noncentrosymmetric semiconductors are spin split by a small amount [39, 40], typically smaller than the energy width of the laser pulse, and so the pulse excites a coherent superposition of the two valence bands, v and v' and two conduction bands, c and c'; we call these states quasi degenerate as we consider their energy separation small. Following [7], these coherences are included by using a multiple scale approach to solve the equation of motion for the single particle density matrix. Therefore, the main idea is to extract an effective dynamics of spinors states $v,\ v'$ in the valence bands and $c,\ c'$ in the conduction bands, where $v,\ v'$ and $c,\ c'$ are spinor states which are quasidegenerate. The key approximations are (i) both hole spins and electron spins contribute to the current. (ii) The energy split between spinors coming from SOC, is small compared with the energy difference between either of the spinors energy, and (iii) the frequency of the optical field is much larger than the energy split between the spinors. With these assumptions, from [7], the equation of motion of the effective density matrix $\rho(\boldsymbol{k};\ t)$ are

$$\frac{\partial \rho_{cc'}(\boldsymbol{k};\ t)}{\partial t} = \frac{e^2}{i\hbar^2}E^a(\omega)E^b(-\omega)\sum_v r^a_{cv}(\boldsymbol{k})r^b_{vc'}(\boldsymbol{k}) \times \left(\frac{1}{\omega - \omega_{c'v}(\boldsymbol{k}) - i0^+} - \frac{1}{\omega - \omega_{cv}(\boldsymbol{k}) + i0^+}\right), \tag{8}$$

and

$$\frac{\partial \rho_{vv'}(\boldsymbol{k};\ t)}{\partial t} = \frac{e^2}{i\hbar^2}E^a(\omega)E^b(-\omega)\sum_c r^a_{cv'}(\boldsymbol{k})r^b_{vc}(\boldsymbol{k}) \times \left(\frac{1}{\omega - \omega_{cv}(\boldsymbol{k}) - i0^+} - \frac{1}{\omega - \omega_{cv'}(\boldsymbol{k}) + i0^+}\right), \tag{9}$$

where $\omega_{nm}(\boldsymbol{k}) = \omega_n(\boldsymbol{k}) - \omega_m(\boldsymbol{k})$, and the denominators clearly indicate the resonance coming from the absorption of a photon with energy $\hbar\omega$, as the electron goes from the valence state v to either of the quasidegenerate states c or c', or as the electron goes from either of the quasidegenerate states v or v', to the conduction state c. In above expressions, $r^a_{nm}(\boldsymbol{k})$ are the matrix elements of $\hat{r}^a$, calculated through the electron velocity,

$$\hat{\boldsymbol{v}} = \dot{\hat{\boldsymbol{r}}} = \frac{1}{i\hbar}[\hat{\boldsymbol{r}},\ H], \tag{10}$$

whose matrix elements lead to $r^a_{nm}(\boldsymbol{k}) = v^a_{nm}(\boldsymbol{k})/(i\omega_{nm}(\boldsymbol{k}))$ with $n \neq m$. From equations (1)–(3) we obtain that $\hat{\boldsymbol{v}} = \hat{\boldsymbol{v}}_0 + \hat{\boldsymbol{v}}_\sigma$, where

$$\hat{\boldsymbol{v}}_0 = -\frac{i}{\hbar}[\hat{\boldsymbol{r}},\ H_0],, \tag{11}$$

is the ordinary electron velocity and

$$\hat{\boldsymbol{v}}_\sigma = -(\hbar\gamma/2)[\hat{\boldsymbol{r}},\ \boldsymbol{\sigma}\cdot\boldsymbol{L}], \tag{12}$$

is the anomalous electron velocity [38].

We measure the spin current through the pseudotensor $\hat{K}^{ab}(\boldsymbol{k})$ proposed in [9] which is given by

$$\hat{K}^{ab}(\boldsymbol{k}) = \frac{1}{2}(\hat{v}^a(\boldsymbol{k})\hat{S}^b(\boldsymbol{k}) + \hat{S}^b(\boldsymbol{k})\hat{v}^a(\boldsymbol{k})), \tag{13}$$

where we allowed for the fact that in general $\hat{\boldsymbol{v}}$ and $\hat{\boldsymbol{S}}$ do not commute in view of equation (12). The expectation value of an observable $\mathcal{O}$ is given by $\mathcal{O} = \mathrm{Tr}(\hat{\rho}\hat{\mathcal{O}})$ where Tr denotes the trace, given by the sum over the diagonal matrix elements, and $\hat{\mathcal{O}}$ is the quantum mechanical operator associated to the observable $\mathcal{O}$. Then, the rate of change of $\mathcal{O}$ is given by $d\mathcal{O}/dt = \dot{\mathcal{O}} = \mathrm{Tr}((d\hat{\rho}/dt)\hat{\mathcal{O}})$. From which we compute the average of the spin current injection tensor $\dot{\boldsymbol{K}}(\boldsymbol{k})$ as

$$\dot{K}^{ab}(\omega) = \int \frac{d^3k}{8\pi^3} \sum_{nn'} \frac{\partial \rho_{nn'}(\boldsymbol{k};\, t)}{\partial t} K^{ab}_{nn'}(\boldsymbol{k}), \tag{14}$$

where we used the closure relationship $|n\boldsymbol{k}\rangle\langle n\boldsymbol{k}| = 1$, and the $\boldsymbol{k}$ integral is over the IBZ. Then, we write

$$\dot{K}^{ab}(\omega) = \mu^{abcd}(\omega) E^{c}(\omega) E^{d}(-\omega), \tag{15}$$

with

$$\mu^{abcd}(\omega) = \mu^{abcd}_{h}(\omega) + \mu^{abcd}_{e}(\omega), \tag{16}$$

where

$$\mu^{abcd}_{h}(\omega) = \frac{\pi e^2}{\hbar^2} \int \frac{d^3k}{8\pi^3} {\sum_{cvv'}}' K^{ab}_{vv'}(\boldsymbol{k}) r^{c}_{cv'}(\boldsymbol{k}) r^{d}_{vc}(\boldsymbol{k}) \times [\delta(\omega - \omega_{cv}(\boldsymbol{k})) + \delta(\omega - \omega_{cv'}(\boldsymbol{k}))], \tag{17}$$

and

$$\mu^{abcd}_{e}(\omega) = \frac{\pi e^2}{\hbar^2} \int \frac{d^3k}{8\pi^3} {\sum_{vcc'}}' K^{ab}_{cc'}(\boldsymbol{k}) r^{c}_{cv}(\boldsymbol{k}) r^{d}_{vc'}(\boldsymbol{k}) \times [\delta(\omega - \omega_{c'v}(\boldsymbol{k})) + \delta(\omega - \omega_{cv}(\boldsymbol{k}))], \tag{18}$$

are the tensorial response functions for the holes (h) and the electrons (e) that characterises the PSC, where the prime symbol of the sums means that v and v' or c and c' are quasi-degenerate conduction states, and the sum only covers these states. Finally,

$$K^{ab}_{nn'}(\boldsymbol{k}) = \frac{1}{2} \sum_{l=v,c} (v^{a}_{nl}(\boldsymbol{k}) S^{b}_{ln'}(\boldsymbol{k}) + S^{b}_{nl}(\boldsymbol{k}) v^{a}_{ln'}(\boldsymbol{k})), \tag{19}$$

are the matrix elements of equation (13). The matrix elements of the spin operator, $\boldsymbol{S}_{nm}(\boldsymbol{k})$, are finite if we include SOC, otherwise they are zero (see appendix (B)).

An important point is that both charge current and net spin density vanish and hence the current is a PSC. For linear polarization, the momentum distribution of carriers is even in $\pm\boldsymbol{k}$. Assuming time reversal symmetry, the velocity is odd in $\boldsymbol{k}$ and hence charge (injection) current vanishes after summation over the whole BZ [14]. Similarly, the spin matrix elements are odd in $\boldsymbol{k}$ and so the net spin density vanishes. The spin current equation (13) however, is even in $\boldsymbol{k}$ and does not vanish under linearly polarized light.

2.1. Spin velocity

To quantify the speed of the particles we define an effective charge velocity as [6, 8]

$$\frac{\hbar}{2} \dot{n}(\omega) \mathfrak{v}^{ab}(\omega) \equiv \dot{K}^{ab}(\omega). \tag{20}$$

$\mathfrak{v}^{ab}$ gives the velocity of electrons along Cartesian direction a with spin polarized along Cartesian direction b. The carrier injection rate $\dot{n}(\omega)$ is [7]

$$\dot{n}(\omega) = \xi^{ab}(\omega) E^{c}(\omega) E^{d}(-\omega), \tag{21}$$

where

$$\xi^{ab}(\omega) = \frac{2\pi e^2}{\hbar^2 V} \int \frac{d^3k}{8\pi^3} \sum_{vc} r^{\mathrm{a}}_{vc}(\boldsymbol{k}) r^{\mathrm{b}}_{cv}(\boldsymbol{k}) \delta(\omega - \omega_{cv}(\boldsymbol{k})), \tag{22}$$

is related to the imaginary part of the linear optical response tensor by $\mathrm{Im}[\epsilon^{ab}(\omega)] = 2\pi\epsilon_0 \hbar \xi^{ab}(\omega)$.

The function $\mathfrak{v}^{ab}(\omega)$ allows us to quantify two very important aspects of PSC. First, we can fix the spin along direction b and calculate the resulting electron velocity. Second, we can fix the velocity of the electron along a and study the resulting direction along which the spin is polarized. In this article we restrict to the first case of the spin polarized along z to take the advantage of the 2D nature of the chosen monochalcogenides, where the spin would then be polarized perpendicular to the plane of the structures as seen in figure 1. To this end, we use an incoming linearly polarized light at normal incidence, and use the direction of the polarized electric field to control $\mathfrak{v}^{ab}(\omega)$. Indeed, writing $\boldsymbol{E}(\omega) = E_0(\omega)(\cos\alpha\, \hat{\mathbf{x}} + \sin\alpha\, \hat{\boldsymbol{y}})$, where α is the polarization angle with respect to x, we obtain from equation (20) that

$$\mathfrak{v}^{xz}(\omega,\, \alpha) = \frac{2}{\hbar} \frac{\mu^{xzxy}(\omega) \sin 2\alpha}{\xi^{xx}(\omega)\cos^2\alpha + \xi^{yy}(\omega)\sin^2\alpha}, \tag{23}$$

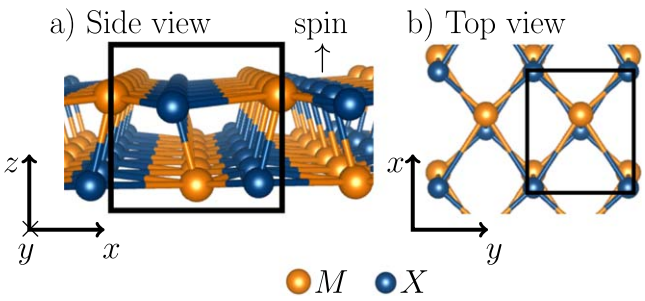

Figure 1. The crystal structure of single-layer group-IV chalcogenides MX, where M = Ge, Sn, and X = S, Se. In (a) we show the 3D view of the single-layer and in (b) the projections of the single-layer crystal on the Cartesian axes. The black rectangles denotes the unit cell. The upward arrow denotes the z direction of the spin.

and

$$\mathfrak{v}^{yz}(\omega,\,\alpha) = \frac{2}{\hbar}\frac{\mu^{yzxx}(\omega)\cos^2\alpha + \mu^{yzyy}(\omega)\sin^2\alpha}{\xi^{xx}(\omega)\cos^2\alpha + \xi^{yy}(\omega)\sin^2\alpha}, \tag{24}$$

where $\mu^{xzxx}(\omega) = \mu^{xzyy}(\omega) = \mu^{yzxy}(\omega) = 0$ due to the $mm2$ point group symmetry of the chosen 2D monochalcogenides; we remark that only the $\mu^{azbc}(\omega)$ are involved for the spin polarized along z. The speed of the injected spin along z is given by

$$\mathfrak{v}^{z}(\omega,\,\alpha) = \sqrt{(\mathfrak{v}^{xz}(\omega,\,\alpha))^2 + (\mathfrak{v}^{yz}(\omega,\,\alpha))^2}\,, \tag{25}$$

that makes an angle $\theta^z(\omega, \alpha)$ with respect to x given by

$$\theta^{z}(\omega,\,\alpha) = \tan^{-1}\left(\frac{\mathfrak{v}^{yz}(\omega,\,\alpha)}{\mathfrak{v}^{xz}(\omega,\,\alpha)}\right). \tag{26}$$

We see that $\mathfrak{v}^{xz}(\omega,\,\alpha)$ and $\mathfrak{v}^{yz}(\omega,\,\alpha)$ have a mirror plane at $\alpha = 90°$ and a period of 180°. We define the figure of merit for the speed of the injected spin along z by

$$v_a^z(\omega) \equiv \mathfrak{v}^{az}(\omega,\,\alpha = \pi/4), \quad a = x,\,y. \tag{27}$$

3. Structures

Bulk monochalcogenide crystals MX (M = Ge, Sn and X = S, Se) are orthorhombic with point group *mmm* and space group *Pnma* (No. 62) [41]. They consist of van der Waals-bonded double layers of metal monochalchogenide atoms in an armchair arrangement. The space group of the bulk crystal contains eight symmetries including a center of inversion which prevents pure spin current (PSC). Upon exfoliation, the resulting single 'double layer' primitive cell has four atoms as seen in figure 1, with the layers chosen perpendicular to the z axis. The single-layer structure has four symmetries, including a two fold rotation with respect to x (plus translation), $2[001] + (1/2, 0, 1/2)$. In addition, the 2D system has two mirror symmetries with respect to z and y, $(1/2, 1/2, 1/2)$ and $m[010] + (0, 1/2, 0)$, that leads to an $mm2$ point group, which determines the nonzero components of the optical response tensors, like $\mu^{abcd}(\omega)$ and $\xi^{ab}(\omega)$. The atomic slab widths are 2.84, 2.73, 2.56 and 2.61 Å for SnS, SnSe, Ges, GeSe respectively.

4. Numerical method

We calculated the self-consistent ground state and the Kohn–Sham states within density functional theory in the independent-particle scheme within the local density approximation (DFT-LDA), with a plane wave basis using the ABINIT code [42]. The Hartwigsen-Goedecker-Hutter (HGH) relativistic separable dual-space Gaussian pseudopotentials [43], are used by ABINIT to include $H_{\rm SOC}$, as given in equation (3), in order to calculate $K^{\rm ab}_{nn'}$ from equation (19). The convergence parameters for the calculations, for all the structures are a cutoff energy of 30Ha, resulting in LDA band gaps of 1.35, 0.80, 1.82 and 1.05 eV for SnS, SnSe, GeS, GeSn, respectively. The TINIBA code [44], was used to calculate the response functions for which 4356 $\boldsymbol{k}$ points in the IBZ were used to integrate $\mu^{abcd}(\omega)$ and $\xi^{ab}(\omega)$ using the linearized analytic tetrahedron method. The $\boldsymbol{k}$ points form a grid of small tetrahedra that covers the volume inside the IBZ where integrand of equation (16) is evaluated at every tetrahedron vertex. For a given frequency ω, the constant energy surface defined by the δ function is then identified inside each tetrahedron, and the surface integral is calculated analytically by linearly interpolating the

integrand over the tetrahedron. We refer the reader to [7] for the details. When calculating equation (13) we neglect the anomalous velocity $\hat{\boldsymbol{v}}_\sigma$ of equation (12), as this term is known to give a small contribution to PSC [6], and thus the velocity operator of the electron $\boldsymbol{v}$ is only given by $\boldsymbol{v}_0$, where $[\hat{\boldsymbol{v}}_0,\ \hat{\boldsymbol{S}}] = 0$, for which equation (13) reduces to $\hat{K}^{ab} = \hat{v}_0^a \hat{S}^b = \hat{S}^b \hat{v}_0^a$.

Finally, the prime in the sum of equations (17) and (18) are restricted to quasi-degenerated valence and conduction bands n and n' that are closer than $\delta c = 30$ meV to each other, which is both the typical laser pulse energy width and the thermal room-temperature energy level broadening [7]. We include 20 valence and 40 conduction bands, which accounts for all allowed transitions up to 6 eV. To model the slabs we use supercells of 20 Å along z, which corresponds to vacuum larger than 17 Å, and renormalize our results to the atomic slab widths mentioned in the previous section, thus removing the vacuum as it must. We mention that with the number of $\boldsymbol{k}$ points and conduction bands, the calculated spectra are accurate at least to within 2 decimal places.

5. Results for SnS

We present results for monolayer SnS, which was experimentally realized recently [37], as a representative example of the four monochalcogenides studied. In the appendix we shows the results for SnSe, GeS and GeSe.

In figure 2, we show as a function of $\hbar\omega$, $\mu^{azbc}(\omega)$, $\xi^{aa}(\omega)$, and $\nu^z_{x,y}(\omega)$ of equations (16), (22), and (27), respectively. The latter gives the figure of merit, for SnS for the SVI (spin-velocity injection), and remark that $\xi^{aa}(\omega)$ is a positive definite function. We only show the results in the visible range, where there are ample sources of devices to produce light of the required energy or its corresponding wavelength $\lambda(\text{nm}) = 1240/\hbar\omega(\text{eV})$. We see that $\nu^z_{x,y}(\omega)$, which is the central result of this article, has a rich structure as a function of $\hbar\omega$, and more importantly, reaches magnitudes (in modulo) around ~500 Km s^{-1}, albeit not necessarily at the same energies; similar values of the SVI were predicted for hydrogenated graphene [8]. Right at the energy gap, we see the onset of $\mu^{azbc}(\omega)$ and $\xi^{aa}(\omega)$, and correspondingly of $\nu^z_{x,y}(\omega)$. There are three energy regions where $\nu^z_{x,y}(\omega)$ is large, around 1.30 eV in the infrared region, between 1.6 and 1.8 eV covering red and around 2.16 eV in the yellow. The behaviour of $\nu^z_{x,y}(\omega)$ versus $\hbar\omega$ could be understood by looking at $\mu^{azbc}(\omega)$ and $\xi^{aa}(\omega)$ (upper panels). For instance, the structure of the almost constant plateau around 1.7 eV which leads to a positive $\nu^z_x(\omega)$ and a larger negative $\nu^z_y(\omega)$ comes directly from the three components of $\mu^{azbc}(\omega)$ and the two of $\xi^{aa}(\omega)$, as all of them have also flat plateaus in that energy region. On the other hand, the structures of $\nu^z_x(\omega)$ and $\nu^z_y(\omega)$ between 1.6 and 1.8 eV and around 2.16 eV come from the interplay of the $\mu^{azbc}(\omega)$ and both $\xi^{xx}(\omega)$ and $\xi^{yy}(\omega)$, as prescribed by equations (23) and (24) at $\alpha = \pi/4$.

We analize the dependence of $\mathfrak{v}^z(\omega,\ \alpha)$ and $\theta^z(\omega, \alpha)$ (equations (25) and (26)), with α, the angle that gives the direction of the linearly polarized electric field of the normally incident beam of light. In general, the following results are obtained from equations (23)–(24) $\mathfrak{v}^{xz}(\omega,\ 0) = 0$, $\mathfrak{v}^{yz}(\omega,\ 0) = (2/\hbar)\mu^{yzxx}/\xi^{xx}$ $\mathfrak{v}^{xz}(\omega,\ 90°) = 0$, and $\mathfrak{v}^{yz}(\omega,\ 90°) = (2/\hbar)\mu^{yzyy}/\xi^{yy}$, from which we can understand the extreme values at $\alpha = 0, 90°$, for the four monochalcogenides of this work.

To analyze $\mathfrak{v}^z(\omega,\ \alpha)$ and $\theta^z(\omega, \alpha)$ we zoom into the three regions of $\hbar\omega$ mentioned above for SnS for which we find not only a large value of the SVI but also an interesting behavior that allows the manipulation of the direction of the SVI itself trough the value of α. In figure 3 (left panel) we show $\mathfrak{v}^z(\omega,\ \alpha)$ and $\theta^z(\omega, \alpha)$ versus α, for $\hbar\omega$ between 1.34 and 1.45 eV (in steps of 0.005 eV) corresponding to the infrared. We notice that for $\alpha \leqslant 30°$, $\mathfrak{v}^z(\omega,\ \alpha)$ is maximum for the chosen values of $\hbar\omega$ and reaching speeds between 200 and 300 Km s^{-1}. For $\alpha \geqslant 30°$, $\mathfrak{v}^z(\omega,\ \alpha)$ decreases by a small amount and is almost constant with roughly the same values of $\mathfrak{v}^z(\omega,\ \alpha)$ for $\alpha \leqslant 30°$. Also, we see that at as we vary α we can go from $\theta^z(\omega, 0) = -90°$ till $\theta^z(\omega, 90) = -90°$ continuously, and that $\theta^z(\omega, \alpha)$ changes by no more that 10° as we vary α from 0° till 90°, thus controlling both the speed and the direction of the PSC. We notice too that the shown results are very similar for all the energies in the chosen interval, and that in particular for 1.34 eV, $\mathfrak{v}^z(\omega,\ \alpha) \sim 310$ Km s^{-1} for all values of α. In the middle panel of figure 3, we show $\mathfrak{v}^z(\omega,\ \alpha)$ and $\theta^z(\omega, \alpha)$ versus α, for $\hbar\omega$ between 1.6 eV and 1.8 eV (in steps of 0.005 eV), corresponding to the red subrange of the visible. For these choices of $\hbar\omega$ we see that the variation of $\mathfrak{v}^z(\omega,\ \alpha)$ versus α grows as α goes from 0° to (90°), reaching speed up to 170 Km s^{-1}. On the other hand the behavior of $\theta^z(\omega, \alpha)$ as a function of α is symmetric around 45° with a maximum deviation of ~10° at $\alpha = 45°$. The qualitative behaviour of this energy range is very similar to the previous one. Finally, in figure 3 (right panel), for chosen values of $\hbar\omega$ in the blue region of the spectrum, we show $\mathfrak{v}^z(\omega,\ \alpha)$, where the maximum speed reaches ~520 Km s^{-1}, and $\theta^z(\omega, \alpha)$ versus α goes from −90° to ~ − 117°. From the bottom panel of figure 2 we clearly see that around $\hbar\omega = 1.600$ eV both $|\nu^z_x|$ and $|\nu^z_y|$ have a sharp maxima, thus giving the large values of $\mathfrak{v}^z(\omega,\ \alpha)$, with the very similar behaviour for both $\mathfrak{v}^z(\omega,\ \alpha)$ and $\theta^z(\omega, \alpha)$ as function of α.

In order to relate the extrapolated spin current velocity to an experimentally observable quantity, we calculate the average distance d by which the up and down spin populations are displaced. From [6] we obtain that $d \sim 4\tau\mathfrak{v}^z(\omega,\ \alpha)$, where τ is the momentum relaxation time. Here, some caveats are necessary. First, for the

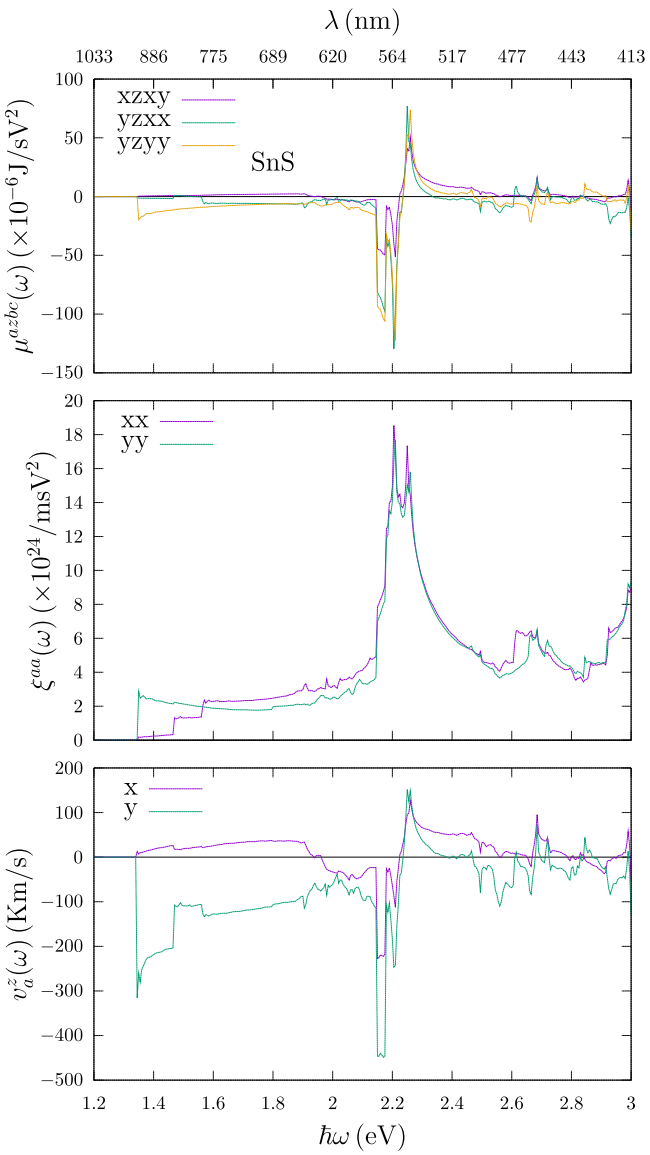

Figure 2. $\mu^{azbc}(\omega)$, $\xi^{aa}(\omega)$, and $\nu^{z}_{(x,y)}(\omega)$ of equations (16), (22), and (27) respectively, versus $\hbar\omega$ for SnS.

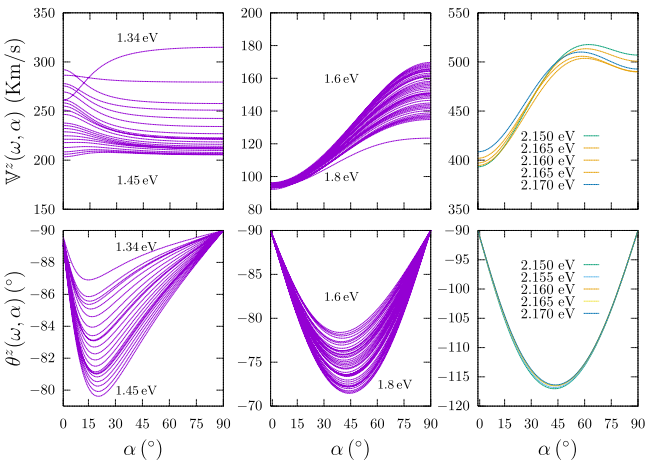

Figure 3. $\mathbb{v}^z(\omega,\ \alpha)$ and $\theta^z(\omega,\alpha)$ of equations (25) and (26), respectively, versus α for SnS.

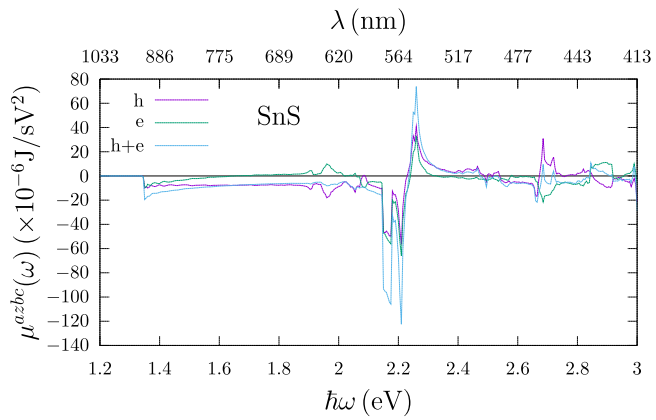

Figure 4. For SnS, hole μ_h^{yzyy} and electron μ_e^{yzyy} contributions to μ^{yzyy}. See equations (16)–(18).

sake of simplicity, we will assume τ to be constant. The constant-relaxation-time approach is a rough approximation to describe globally the carrier scattering processes by electron-electron, electron-phonon, electron-impurity etc., interactions which, however, depend on the material, the doping level and the temperature. More in general, the relaxation time varies with the band energy and the quasimomentum. But all this is beyond the scope of this work and this approximation can still give in general a reasonable estimate in most of the cases of our interest, where temperature, anisotropy and hole-electron differences are neglected [17, 36, 45, 46]. Several papers tried to evaluate the momentum relaxation time of monochalcogenides, both bulk [47, 46, 48, 49], and 2D systems [17, 36, 50, 51]. Moreover, theoretical calculations based on simple models or more refined *ab initio* approaches on single-layer SnS [36], SnSe [50], and GeSe [51], take into account a range of values for τ spanning from roughly 10 to 1000 fs, depending on the calculated band energies (*ab initio*, at T = 0), up to 3eV above the Fermi level, and lattice temperatures (to which the relaxation time is inversely proportional) roughly considered between 300 to 600 K. Thus, keeping all this in mind and considering for τ the range 10–1000 fs, from figure 3 we see that $\mathbb{v}^z(\omega,\ \alpha = 90°) \sim 500$ Km s^{-1} for $\hbar\omega = 2.160$ eV and then $d \sim 20 - 2000$ nm. This value of d could be ∼1 and up to ∼100 times larger than those experimentally measured values of $d = 20$ nm for GaAs [16], AlGaAs [16] and $d = 24$ nm for ZnSe [17],. Also, from figure 9 we mention that $|\mu^{yzyy}|$ of SnS is $\sim 20 \times |\mu^{xxxx}|$ of GaAs, where in general the monochalcogenides have much larger values of μ^{abcd} than those of bulk semiconductors, making the SnS, SnSe, GeS and GeSe monochalcogenides, excellent structures for the realization of PSC.

In figure 4 we show the h-hole μ_h^{yzyy} and the e-electron μ_e^{yzyy} contributions of equations (17) and (18), to μ^{yzyy} of equation (16). We see that from 1.7 to 2.1 and above 2.5 eV both contributions partially cancel each other. However, we see that for $\hbar\omega$ below $1.7eV$ and around 2.2 eV both contributions add up, giving the large μ^{yzyy} value that leads to the high velocities shown in figures 2 and 3 for the corresponding energy ranges.

In the appendix A we present the results for SnSe, GeS and GeSe. It is worth mentioning that in particular for SnSe as seen in figure 5 we find six $\hbar\omega$ regions where v_x^z and v_y^z have the same sign, thus adding up to the very large values of $\mathbb{V}^z(\alpha,\ \omega)$ shown in figure 6. In summary, we find that each structure has as a function of $\hbar\omega$ a rich variety of SVI that reaches values as high as ∼520 Km s^{-1} for SnS, ∼360 Km s^{-1} for SnSe, ∼280 Km s^{-1} for GeS and ∼360 Km s^{-1} for GeSe, and by changing the direction of the linearly polarized electric field that induces SVI, its direction could be controlled, thus giving ample possibilities to manipulate it at will. The large SVI values in turn lead to average distances that the up-spins are separated from the down-spins in the PSC, which are ∼20 larger than for those of bulk semiconductors where it has been experimentally measured [15–17], giving a larger physical space for applications, like gates that could detect the PSC. In particular we found that for SnSe there are energies of the incoming light for which one can inject z-polarized spins along the y surface direction regardless of the polarization angle α of the linearly polarized light, thus opening the possibility of having SVI for unpolarized light. We remark that SnSe is more sensitive to selected wavelengths than the other materials studied here. Finally, in Appendixes C and D we discuss the role of coherences, band structure and the Projected Density of States (PDOS) towards the PSC, taking above results for SnS as an example.

6. Summary of main results

In table 1 we summarize the results for the highest values of $\mathbb{v}^z(\omega,\ \alpha)$ (equation (25)) and its subsequent angle $\theta^z(\omega, \alpha)$ (equation (26)) for the four monochalcogenides studied in this work. We see that for SnS (figure 3)

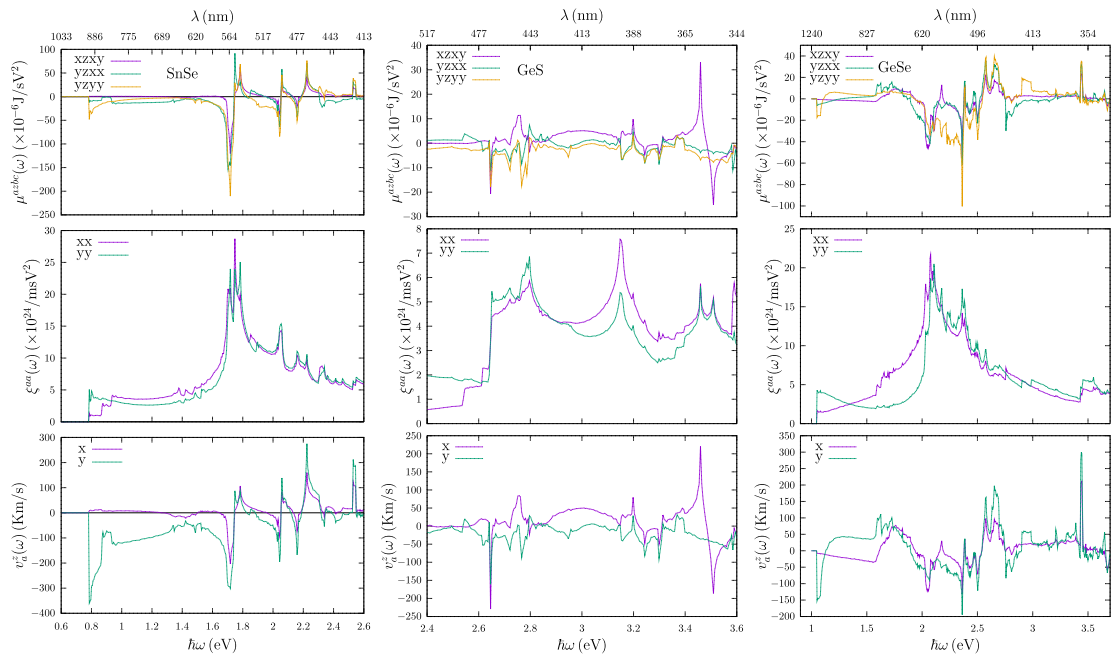

Figure 5. $\mu^{azbc}(\omega)$, $\xi^{aa}(\omega)$, and $v^{z}_{(x,y)}(\omega)$ of equations (16), (22), (27) respectively, versus $\hbar\omega$ for SnSe, GeS and GeSe.

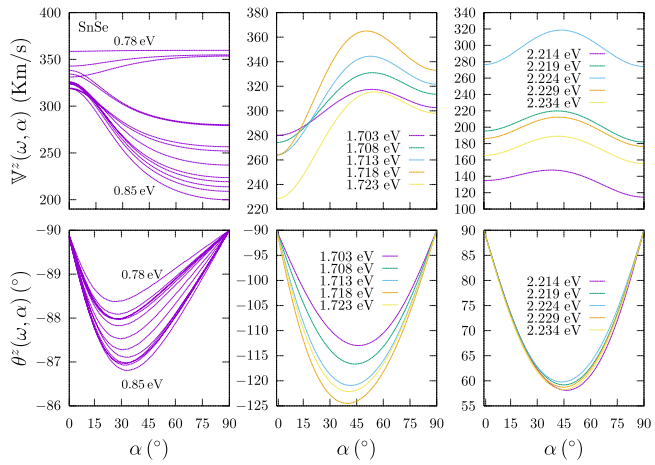

Figure 6. $\mathbb{v}^{z}(\omega,\ \alpha)$ and $\theta^{z}(\omega,\alpha)$ of equations (25) and (26), respectively, versus α for SnSe.

Table 1. Theoretical lattice constant a_0 and LDA band gap energy E_g of the monochalcogenides studied in this work, along with their corresponding maxima of $\mathbb{v}^{z}_{\max}$ (equation (25)) and the direction angle θ^{z} (equation (26)) for the spin polarized along z. The values of $\hbar\omega$ and polarization angle α of the incoming polarized electric field for $\mathbb{v}^{z}_{\max}(\omega,\ \alpha)$ are also given.

	a_0 (Bohrs)	Gap (eV)	$\mathbb{v}^{z}_{\max}$ (Km s^{-1})	θ^{z}	$\hbar\omega$ (eV)	α
SnS	4.1103	1.35	520	$-110°$	2.15	60°
SnSe	4.3104	0.80	360	$-90°$	0.80	$0 \rightarrow 90°$
GeS	3.6573	1.82	270	$-135°$	2.646	45°
GeSe	4.9793	1.05	370	55°	3.438	45°

$\mathbb{v}^{z}_{\max}(\omega,\ \alpha) = 520$ Km s^{-1} at $\hbar\omega = 2.15$ eV or yellow part of the visible spectrum and $\alpha = 60°$ with $\theta^{z} = -110°$, and the electric field polarized at $\alpha = 60°$ with respect to x; for GeS (figure 7) $\mathbb{v}^{z}_{\max}(\omega,\ \alpha) = 270$ Km s^{-1} at $\hbar\omega = 2.646$ eV or blue part of the visible spectrum and $\alpha = 45°$ with $\theta^{z} = -135°$, and the electric field polarized at $\alpha = 45°$ with respect to x; for GeSe (figure 8) $\mathbb{v}^{z}_{\max}(\omega,\ \alpha) = 370$ Km s^{-1} at $\hbar\omega = 3.438$ eV or ultraviolet part

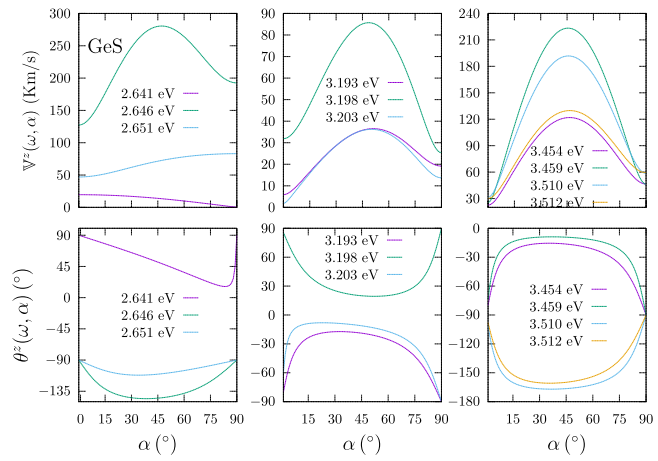

Figure 7. $\mathbb{v}^z(\omega,\ \alpha)$ and $\theta^z(\omega,\alpha)$ of equations (25) and (26), respectively, versus α for GeS.

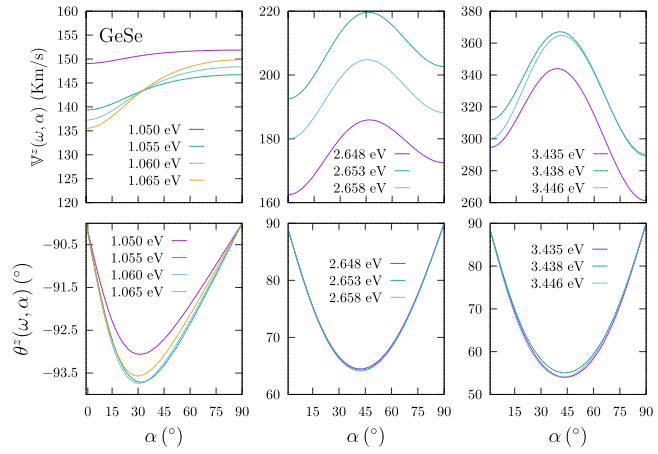

Figure 8. $\mathbb{v}^z(\omega,\ \alpha)$ and $\theta^z(\omega,\alpha)$ of equations (25) and (26), respectively, versus α for GeSe.

of the spectrum and $\alpha = 45°$ with $\theta^z = 55°$, and the electric field polarized at $\alpha = 45°$ with respect to x. It is interesting to see that for SnSe (figure 6) $\mathbb{v}^z_{\max}(\omega,\ \alpha) = 360$ Km s^{-1} right at its band gap of $\hbar\omega = 0.80$ eV which is in the infrared part of the spectrum and $\alpha = 45°$ with $\theta^z = 55°$, where we remark that the electric field could be polarized from $\alpha = 0°$ to $\alpha = 90°$ with respect to x, keeping the same values of $\mathbb{v}^z_{\max}$ and θ^z, which would mean that unpolarized light could be used in this case. From figures 2 and 5 it should be clear that there is no obvious explicit pattern in the $\mathbb{v}^z(\omega)$ as we go through the SnS, SenSe, GeS and GeSe monochalcogenides. Of course it would be interesting to understand the detail PSC physics behind the changing of S and Se atoms in Sn and Ge. For instance one could envision a layer by layer analysis of the two layers that conform the monochalcogenides (figure 1) following the scheme developed in [52–55], in order to elucidate the role of each atomic species at each layer towards their contribution to $\mu^{abcd}_{h,e}(\omega)$ (equations (17)–(18)), taking special care of the spin degree of freedom. This is a research topic with its own merits but it is out of the scope of the present article, where its main goal was to demonstrate that single-layer SnS, SnSe, GeS and GeSe are excelent candidates to produce on demand spin-current for spintronics applications.

7. Conclusions

Using novel single-layer 2D monochalcogenides, SnS, SnSe, GeS, and GeSe, we have shown that these 2D films are excellent candidates for spin current injection. In particular, we reported the results of *ab initio* calculations for the spin velocity injection (SVI) due to one-photon absorption of the linearly polarized light as a function of its energy and direction of polarization. The theoretical formalism to calculate the SVI includes the excited coherent superposition of the spin-split conduction bands that arise in the noncentrosymmetric structures considered here. We made the calculations for the cases when the spin is polarized in the z direction that is

perpendicular to the 2D films and study the resulting SVI velocity along the x or y directions parallel to the films. We have shown that the SVI display an interesting behavior, which depends upon the material, but where we found similarities in that all of them show values around and above 150 Km s^{-1} for the SVI, with an ample control of the direction of the SVI through the manipulation of the angle α of the linearly polarized light. Also, the particularities of each material made these structures excellent spintonic candidates. In particular we found that for SnSe there are energies of the incoming light for which one can inject z-polarized spins along the y surface direction regardless of the polarization angle α of the linearly polarized light, thus opening the possibility of having SVI for unpolarized light.

The speed values obtained here are of the same order of magnitude as those of [10] in unbiased semiconductor quantum well structures, and [8] in hydrogenated graphene structures, while they are an order of magnitude higher compared to 3D bulk materials. Moreover, the distance d by which the spin up and spin down populations are separated is larger than for other semiconductors where d has been measured [16, 17]. Therefore, the 2D monochalcogenide structures considered here are excellent candidates for the development of spintronics devices that require pure spin current (PSC).

Acknowledgments

L.J.R. acknowledges support from CONACyT through a postdoctoral research fellowship while at the Centro en Investigaciones en Óptica, A.C., currently unemployed. B.S.M. acknowledges the support from CONACyT through grant A1-S-9410. B.M.F. thanks NSF DMR-2015639 and NERSC-DOE-AC02-05CH11231 for their support.

Data availability statement

All data that support the findings of this study are included within the article (and any supplementary files).

Appendix A. Results for SnSe, GeS and GeSe

We go over the results for SnSe, GeS and GeSe, which qualitatively are very similar to those presented for SnS. However, we point out only the most relevant features, since the detailed explanation could be done following that of SnS.

In figure 5 we show as a function $\hbar\omega$, for SnSe, GeS, and GeSe, $\mu^{azbc}(\omega)$, $\xi^{aa}(\omega)$, and $\nu^{z}_{(x,y)}(\omega)$ of equations (16), (22), and equation (27), of the main text, respectively. We see that $\nu^{z}_{x,y}(\omega)$, for each structure has an interesting behaviour as a function of $\hbar\omega$, reaching maximum values around -300, ± 200, and 250 Km s^{-1} for SnSe, GeS and GeSe, respectively, each at different regions of $\hbar\omega$.

As for SnS, we identify three energy regions for each structure where $\nu^{z}_{x,y}(\omega)$ are large. For SnSe the $\hbar\omega$ regions are around 0.8 eV in the infrared, 1.715 eV in the red and 2.22 eV in the green regions of the spectrum. Then, for GeS we have $\hbar\omega \sim 2.6$ eV in the blue, 3.20 eV and 3.5 eV in the near UV. Finally, for GeSe we have $\hbar\omega \sim 1.05$ eV in the infrared, 2.65 eV in the blue, and 3.4 eV in the near UV. As explained in the main text for SnS, the features seen in $\nu^{z}_{(x,y)}(\omega)$ readily come from the interplay of $\mu^{azbc}(\omega)$ and $\xi^{aa}(\omega)$ shown in the upper panels of the corresponding figure for each system, from where they can be deduced in detail.

From equations (25) and (26) we analize $\mathbb{v}^{z}(\omega,\ \alpha)$ and $\theta^{z}(\omega, \alpha)$ versus α, which is the angle that gives the direction of the linearly polarized electric field of the normally incident beam of light. As for SnS, these quantities also shows a very interesting behaviour for SnSe, GeS and GeSe, as seen in figures 6 for SnSe, 7 for GeS and 8 for GeSe, where each panel corresponds to the energy regions given in the previous paragraph for each system. We find very large values of the SVI and also an interesting behavior that allows the manipulation of the direction of the SVI itself trough the value of α, just as explained in the main text for SnS. For instance we see that for SnSe at 0.78 eV (figure 6), the velocity $\mathbb{v}^{z}(\omega,\ \alpha)$ (equation (27))) is constant and the direction of the resulting SVI $\theta^{z}(\omega, \alpha) \sim 90^{\circ}$ is almost independent of α. Going through the results of GeS and GeSe we can find similar behavior, and in general we see that the single-layer 2D monochalcogenides SnS, SnSe, GeS, and GeSe, offer a wide set of possibilities to manipulate with linearly polarized light the spin-velocity injection (SVI) of a pure spin current (PSC).

Appendix B. Matrix element of $\hat{S}$

Form equation (5) the matrix elements of $\hat{\mathbf{S}}$ are given by

$$S^a_{nm}(\boldsymbol{k}) = \frac{\hbar}{2}\int d^3r(\psi^{*(1)}_{n\boldsymbol{k}}(\boldsymbol{r}),\ \psi^{*(2)}_{n\boldsymbol{r}}(\boldsymbol{r}))\sigma^a\begin{pmatrix}\psi^{(1)}_{n\boldsymbol{k}}(\boldsymbol{r})\\ \psi^{(2)}_{n\boldsymbol{k}}(\boldsymbol{r})\end{pmatrix}, \tag{B1}$$

where using the well known σ^a Pauli matrices leads to

$$S^x_{nm}(\boldsymbol{k}) = \frac{\hbar}{2}\int d^3r(\psi^{*(1)}_{n\boldsymbol{k}}(\boldsymbol{r})\psi^{(2)}_{m\boldsymbol{k}}(\boldsymbol{r}) + \psi^{*(2)}_{n\boldsymbol{k}}(\boldsymbol{r})\psi^{(1)}_{m\boldsymbol{k}}(\boldsymbol{r})), \tag{B2}$$

$$S^y_{nm}(\boldsymbol{k}) = i\frac{\hbar}{2}\int d^3r(-\psi^{*(1)}_{n\boldsymbol{k}}(\boldsymbol{r})\psi^{(2)}_{m\boldsymbol{k}}(\boldsymbol{r}) + \psi^{*(2)}_{n\boldsymbol{k}}(\boldsymbol{r})\psi^{(1)}_{m\boldsymbol{k}}(\boldsymbol{r})), \tag{B3}$$

and

$$S^z_{nm}(\boldsymbol{k}) = \frac{\hbar}{2}\int d^3r(\psi^{*(1)}_{n\boldsymbol{k}}(\boldsymbol{r})\psi^{(1)}_{m\boldsymbol{k}}(\boldsymbol{r}) - \psi^{*(2)}_{n\boldsymbol{k}}(\boldsymbol{r})\psi^{(2)}_{m\boldsymbol{k}}(\boldsymbol{r})). \tag{B4}$$

In the absence of SOC, equation (5) reduces to

$$\langle\boldsymbol{r}|n\boldsymbol{k}\rangle = \begin{pmatrix}\psi_{n\boldsymbol{k}}(\boldsymbol{r})\\ 0\end{pmatrix}, \tag{B5}$$

or

$$\langle\boldsymbol{r}|n\boldsymbol{k}\rangle = \begin{pmatrix}0\\ \psi_{n\boldsymbol{k}}(\boldsymbol{r})\end{pmatrix}, \tag{B6}$$

where $\psi^{(1)}_{n\boldsymbol{k}}(\boldsymbol{r}) = \psi^{(2)}_{n\boldsymbol{k}}(\boldsymbol{r}) = \psi_{n\boldsymbol{k}}(\boldsymbol{r})$. From equations (B2)-(B4) it follows that in the absence of SOC, $S^a_{nm}(\boldsymbol{k}) = 0$.

Appendix C. Role of coherences

To understand the role of the coherences for SnS we take as an example the conduction band contribution to its largest component of $\mu^{abcd}(\omega)$, $\mu^{yzyy}(\omega)$, and plot it in figure 9 as a function of δc, which is the maximum energy difference of the quasi-degenerated conduction bands c and c' used in the sum of equation (16). We see that $\mu^{yzyy}(\omega)$ for $\delta c = 0$ eV and $\delta c = 0.03$ eV is basically the same and that for $\delta c = 0.1$ eV the difference is only marginal. To contrast this behavior with respect to δc, we take as a representative example of bulk semiconductors, GaAs. In the bottom panel of figure 9 we show the largest component of $\mu^{abcd}(\omega)$ for GaAs, $\mu^{aaaa}(\omega)$ (with $a = x, y, z$), where now there is a sizable difference among the three values of δc. We see that $\mu^{aaaa}(\omega)$ for $\delta c = 0.03$ eV is a factor of ~2 larger than $\mu^{aaaa}(\omega)$ for $\delta c = 0$, justifying the need of including the coherences. Since we ascribe the value of δc to both a typical laser pulse energy width and/or the thermal room-temperature energy level broadening [7], the value of $\delta c = 0.1$ eV may not be physically meaningful, but we show it for completness of our explanation.

To explain where this behaviour as a function of δc comes from, in the top panel of figure 10 we show the band structure of GaAs, where the arrows represent the transition involved around 2.02 eV and go from spin split valence bands to the spin split conduction bands. At 2.02 eV $|\mu^{aaaa}(\omega)|$ is maximum as seen in figure 9. The purple line is the energy difference between the spin split conduction bands, that are degenerated along L-Γ-X and spin split along X-K-Γ, and the black horizontal line is at $\delta c = 0.03$ eV. From these two lines it follows that along K-Γ there are transitions from c to c' states that would be only included if δc is finite, otherwise only the transition along L-Γ-X, would be the ones that contribute to μ^{abcd}, resulting in the results shown in figure 9. In figure 10, we show the band structure of SnS, where the arrows represent the transition involved around 1.72 eV and go from spin split valence bands to the spin split conduction bands. The purple line is the energy difference between the spin split conduction bands, that are spin split along Γ-X-S, and degenerated along Y-Γ, and the purple line is at $\delta c = 0.03$ eV. In contrast to GaAs, we see that the purple line is above the black line, and thus the value of δc would be irrelevant for SnS, since theses transitions would be included in equations (17) and (18) any way. For the coherences to be seen in SnS, δc would need to be larger than 0.03 eV, but even for $\delta c = 0.1$ eV, as shown in figure 9 the differences are marginal. Indeed, even for 0.1 eV, most of the transitions along Γ-X would also contribute. Equivalent results for the valence bands contribution lead to the same conclusions. Including the coherences is in general important, since otherwise one could be underestimating the value of μ^{abcd} as in the case of GaAs, and if the band structure of the system in question, is like the ones of our single-layer monochalcogenides, the calculation of μ^{abcd} would be insensitive to the coherences.

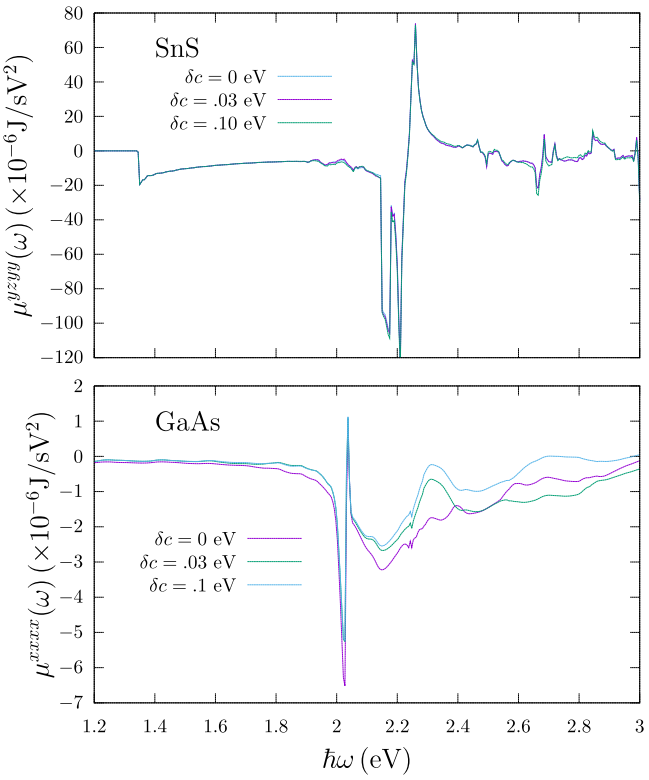

Figure 9. μ^{abcd} for SnS (top panel) and GaAs (bottom panel) for $\delta c = 0, 0.03$ and 0.1 eV, where δc is the maximum energy difference of the quasi-degenerated conduction bands c and c' used in equation (16). Notice that $|\mu^{yzyy}|$ of SnS is $\sim$100 $\times$ $|\mu^{xxxx}|$ of GaAs.

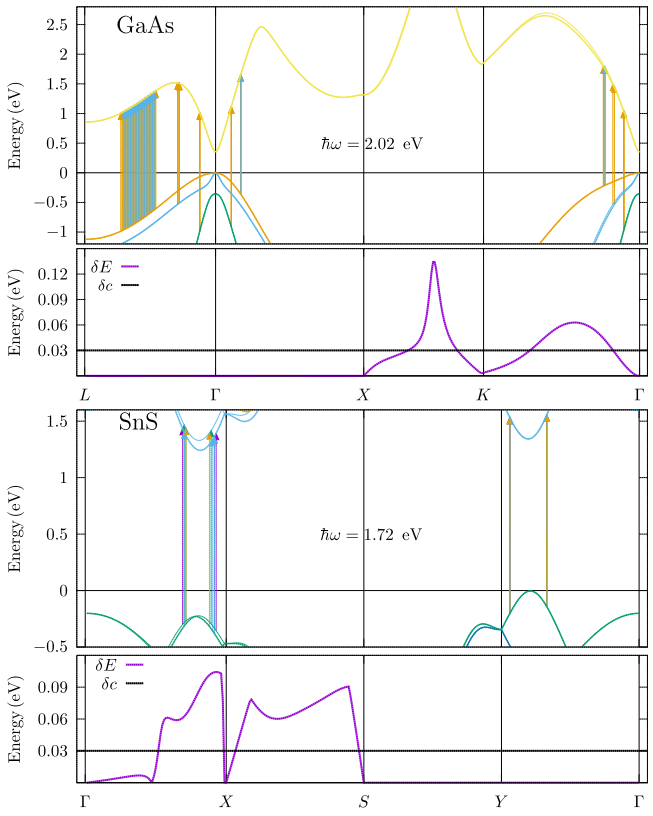

Figure 10. Electronic Band structure of GaAs (top panel) and SnS along the high-symmetry lines of the Irreducible Brillouin Zone (IBZ). Each spin split band has the same color and the thick (thin) line has lower (higer) energy. The arrows represent the transition involved around the energies shown for each structure and go from spin split valence bands to the spin split conduction bands. The zero of energy was set at the highest filled band. See the text for details.

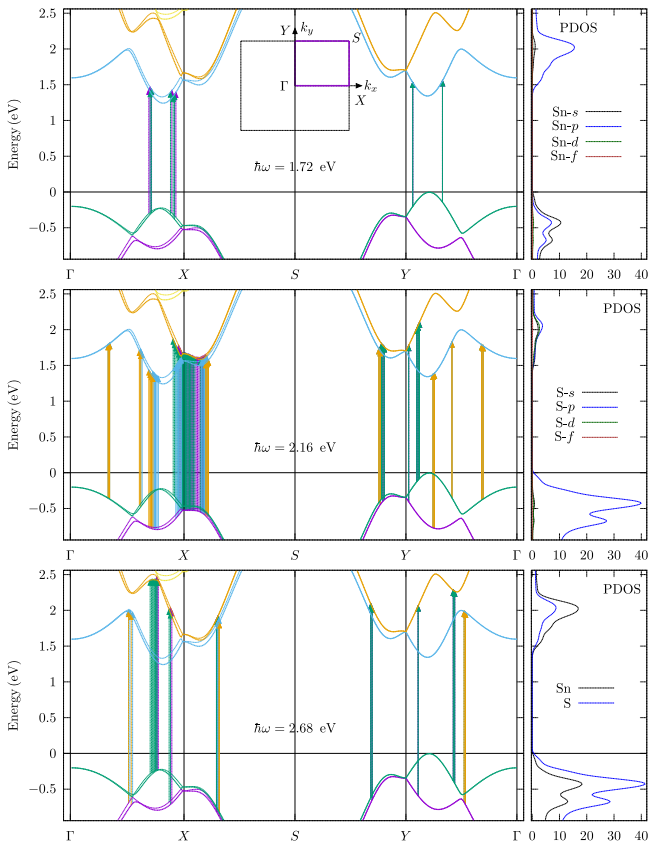

Figure 11. Left panels: Electronic band structure along the high-symmetry lines of the Irreducible Brillouin Zone (IBZ), corresponding to the 2D crystalline structure of SnS. Each spin split band has the same color and the thick (thin) line has lower (higer) energy. The arrows represent the transition involved around the energies of the results shown in figure 3, and go from spin split valence bands to the spin split conduction bands. Right panels: Projected Density of States (PDOS), in arbitrary units, where the top, middle and bottom, panels show the PDOS decomposition into *s*, *p*, *d* and *f* orbitals for Sn, S and the total contribution. The zero of energy was set at the highest filled band. See the text for details.

Appendix D. Band structure and PDOS of SnS

In order to gain understanding from the electronic band structure, in figure 11 we show the structure for SnS, for the energies shown in figure 3. For $\hbar\omega \sim 1.72$ eV we see two regions of transitions, one closer to X in the Γ to X path, and the other closer to Y in the Y to Γ path. All these transitions go from the spin split top most valence (v) band to the first spin split conduction (c) band. When the splitting of the bands is large, as it is below X, one can see that the green arrow point to the lower c spin split band, whereas the purple arrow point to the higher c spin split band. On the other hand, we see that when the splitting is zero, as it happens for the bands from Y to Γ, only two arrows are present, however these two arrows contain overlapping arrows representing a number of transitions similar to those below X. Then, this similarity in the number and position within the IBZ of above transitions is related to the same direction and magnitude seen in $v_a^z(\omega)$ of figure 2 for this energy region.

To understand the orbital character of the electronic transitions involved in the results, we show in the right panels of figure 11, the Projected Density of States (PDOS) for SnS, where the top, middle and bottom panels are for Sn, S, and the total (S+Sn) PDOS contribution. We see that the occupied states are dominated by the *s* and *p* orbitals of Sn along with the *p* orbitals of S, where the contributions form *d* and *f* orbitals is negligible for both atoms. For the unfilled or empty sates, the *p* orbital of Sn dominate and the *s*, *p* and *d* orbitals of S are similar to each other, however their PDOS is much smaller than that of Sn. The total PDOS, i.e. the sum of $s + p + d + f$, shows a larger value for the occupied states of S than those of Sn, and a larger value for the empty states of Sn than those of S. Then, we would expect to have more electronic transitions from the occupied orbitals of S to the empty orbitals of Sn. To analyze this feature with more detail, in figure 12 we decompose the PDOS for all the possible combinations of the *s* and *p* orbitals for both Sn and S, where in order to be more specific, we study the origin of the electronic transitons around $\hbar\omega \sim 1.72$ eV. In figure 12 we show these transitions with blue lines connecting the occupied states with the empty states, where these lines could have any slope and should not be confused with the vertical arrows of figure 11 that denote vertical optical transitions that conserve $\boldsymbol{k}$. We point out that one needs a finite PDOS both in the occupied states and the empty states for the electronic transitions to

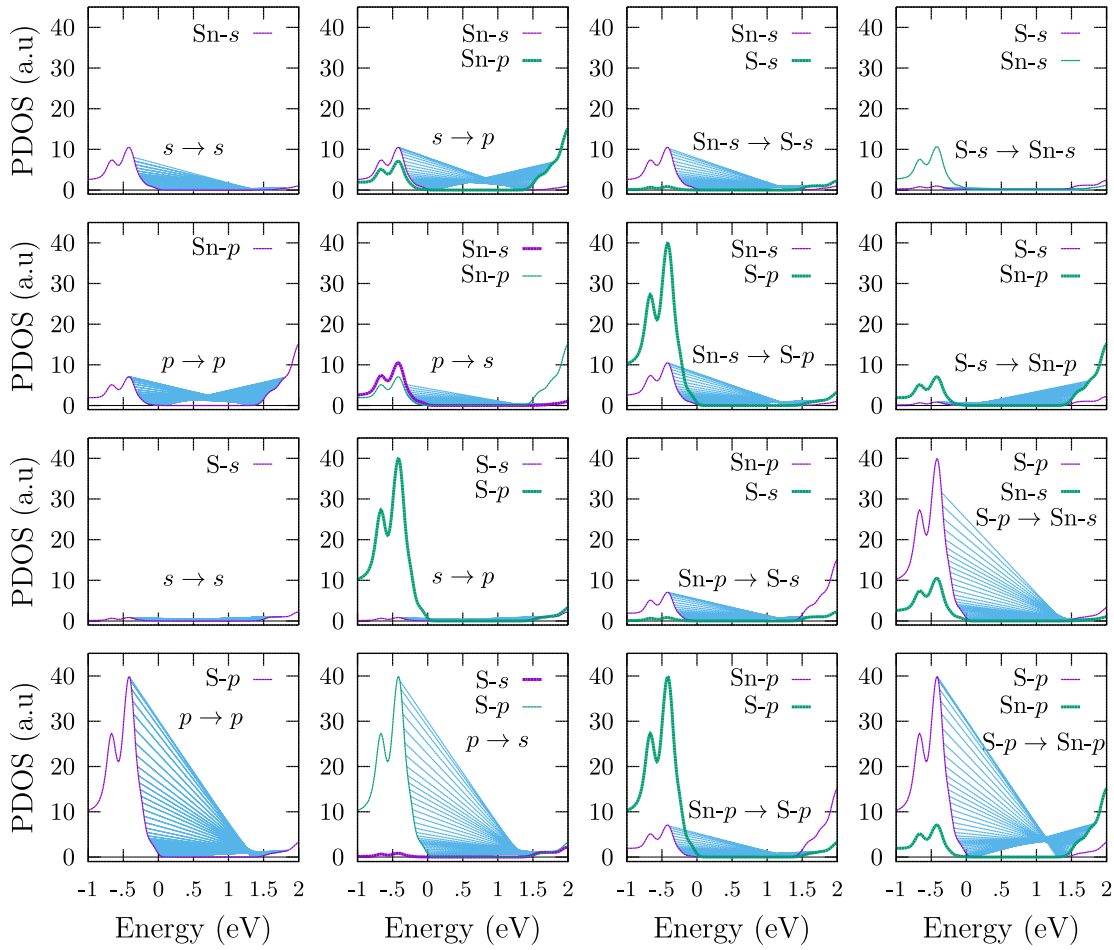

Figure 12. Projected Density of States (PDOS), in arbitrary units, corresponding to the 2D crystalline structure of SnS. The blue lines represent the transition involved around $\hbar\omega = 1.72$ eV of the results shown in the left panel of figure 3. The zero of energy was set at the highest occupied band. See the text for details.

take place. Therefore, we see that the transitions that contribute the most are Sn-p→Sn-p transitions, that are similar to Sn-s→Sn-p transitions, and S-p→Sn-p transitions which are the largest. The rest of the transitions have a negligible or very small PDOS, either in the occupied or empty states, or both. Thus, are the former set of transition the ones that contribute to the spectra seen in figure 2 around $\hbar\omega = 1.72$ eV. A similar study for the other energy regions of figure 3 or those of SnSe, GeS and GeSe, in figures 6, 7 and 8, respectively, lead to the same qualitative analysis. In summary, the PDOS is composed by a rich structure of transitions among orbital states, that include both intraatomic and interatomic combinations of *s* and *p* orbitals.

ORCID iDs

Bernardo S Mendoza https://orcid.org/0000-0002-8546-0262
Benjamin M Fregoso https://orcid.org/0000-0002-8417-7430

References

[1] Wolf S A, Awschalom D D, Buhrman R A, Daughton J M, Von Molnar S, Roukes M L, Chtchelkanova A Y and Treger D M 2001 *Science* **294** 1488
[2] Awschalom D D and Flatté M E 2007 *Nat. Phys.* **3** 153
[3] Fabian J, Matos-Abiague A, Ertler C, Stano P and Zutic I 2007 *Ac. Phys. Slov.* **57** 565
[4] Awschalom D D, Loss D and Samarth N 2011 *Semiconductor Spintronics and Quantum Computation* (Berlin, London: Springer)
[5] Sinova J, Culcer D, Niu Q, Sinitsyn N A, Jungwirth T and MacDonald A H 2004 *Phys. Rev. Lett.* **92** 126603
[6] Bhat R D R, Nastos F, Najmaie A and Sipe J E 2005 *Phys. Rev. Lett.* **94** 096603
[7] Nastos F, Rioux J, Strimas-Mackey M, Mendoza B S and Sipe J E 2007 *Phys. Rev.* B **76** 205113
[8] Zapata-Peña R, Mendoza B S and Shkrebtii A I 2017 *Phys. Rev.* B **96** 195415
[9] Bhat R D R and Sipe J E 2000 *Phys. Rev. Lett.* **85** 5432
[10] Najmaie A, Bhat R D R and Sipe J E 2003 *Phys. Rev.* B **68** 165348

[11] Bhat R D R, Nemec P, Kerachian Y, van Driel H M and Sipe J E 2005 *Phys. Rev.* B **71** 035209
[12] Alvarado S F, Riechert H and Christensen N E 1985 *Phys. Rev. Lett.* **55** 2716
[13] Schmiedeskamp B, Vogt B and Heinzmann U 1988 *Phys. Rev. Lett.* **60** 651
[14] Fregoso B M 2019 *Phys. Rev.* B **100** 064301
[15] Zhao H, Loren E, Driel H V and Smirl A 2006 *Phys. Rev. Lett.* **96** 246601
[16] Stevens M J, Smirl A L, Bhat R D R, Najmaie A, Sipe J E and Van Driel H M 2003 *Phys. Rev. Lett.* **90** 136603
[17] Hübner J, Rühle W W, Klude M, Hommel D, Bhat R D R, Sipe J E and van Driel H M 2003 *Phys. Rev. Lett.* **90** 216601
[18] Kimura T, Hashimoto N, Yamada S, Miyao M and Hamaya K 2012 *NPG Asia Mat.* **4** e9
[19] Murakami S, Nagaosa N and Zhang S C 2003 *Science* **301** 1348
[20] Majumdar S, Laiho R, Laukkanen P, Väyrynen I J, Majumdar H S and Österbacka R 2006 *App. Phys. Lett.* **89** 122114
[21] Datta S and Das B 1990 *App. Phys. Lett.* **56** 665
[22] Götte M, Joppe M and Dahm T 2016 *Sci. Rep.* **6** 36070
[23] Pershin Y V and Di Ventra M 2008 *Phys. Rev.* B **78** 113309
[24] Li L, Chen Z, Hu Y, Wang X, Zhang T, Chen W and Wang Q 2013 *J. Am. Chem. Soc.* **135** 1213
[25] Singh A K and Hennig R G 2014 *Appl. Phys. Lett.* **105** 042103
[26] Wang F, Young S M, Zheng F, Grinberg I and Rappe A M 2016 *Nat. Commun.* **7** 10419
[27] Ramasamy P, Kwak D, Lim D-H, Ra H-S and Lee J-S 2016 *J. Mater. Chem.* C **4** 479
[28] Wu M and Zeng X C 2016 *Nano Lett.* **16** 3236
[29] Kamal C, Chakrabarti A and Ezawa M 2016 *Phys. Rev.* B **93** 125428
[30] Guo S-D and Wang Y-H 2017 *J. Appl. Phys.* **121** 034302
[31] Xin C, Zheng J, Su Y, Li S, Zhang B, Feng Y and Pan F 2016 *J. Phys. Chem.* C **120** 22663
[32] Hanakata P Z, Carvalho A, Campbell D K and Park H S 2016 *Phys. Rev.* B **94** 035304
[33] Rangel T, Fregoso B M, Mendoza B S, Morimoto T, Moore J E and Neaton J B 2017 *Phys. Rev. Lett.* **119** 067402
[34] Mendoza B S and Fregoso B M 2020 *Phys. Rev.* B **102** 195410
[35] Li-Dong Zhao S-H L, Zhang Y, Sun H, Tan G, Uher C, Wolverton C, Dravid V P and Kanatzidis M G 2014 *Nature* **508** 373
[36] Gupta R, Dongre B, Carrete J and Bera C 2021 *J. Appl. Phys.* **130** 054301
[37] Higashitarumizu N, Kawamoto H, Lee C-J, Lin B-H, Chu F-H, Yonemori I, Nishimura T, Wakabayashi K, Chang W-H and Nagashio K 2020 *Nat. Commun.* **11** 2428
[38] Spavieri G and Mansuripur M 2015 *Phys. Scr.* **90** 085501
[39] Dresselhaus G 1955 *Phys. Rev.* **100** 580
[40] Chantis A N, van Schilfgaarde M and Kotani T 2006 *Phys. Rev. Lett.* **96** 086405
[41] International Tables for Crystallography
[42] Gonze X *et al* 2009 *Comput. Phys. Commun.* **180** 2582
[43] Hartwigsen C, Goedecker S and Hutter J 1998 *Phys. Rev.* B **58** 3641
[44] Mendoza B S, Anderson S M, Cabellos J L and Rangel T 2011 TINIBA: *Ab initio* calculation of the optical properties of solids, surfaces, interfaces, and 2D materials (INDAUTOR-México No. 03-2009-14033400-01)
[45] Albers W, Haas C, Vink H J and Wasscher J D 1961 *J. Appl. Phys.* **32** 2220
[46] Shi G and Kioupakis E 2015 *J. Appl. Phys.* **117** 065103
[47] Nassary M 2005 *J. Alloys Compd.* **398** 21
[48] González-Romero R L, Antonelli A and Meléndez J J 2017 *Phys. Chem. Chem. Phys.* **19** 12084
[49] Fan Q, Yang J, Cao J and Liu C 2021 *Royal Society Open Science* **8** 201980
[50] Ding G, Hu Y, Li D and Wang X 2019 *Results in Physics* **15** 102631
[51] Li Y, Ma K, Fan X, Liu F, Li J and Xie H 2020 *Appl. Surf. Sci.* **521** 146256
[52] Castillo C, Mendoza B S, Schmidt W, Hahn P and Bechstedt F 2003 *Phys. Rev. B Rapid Communications* **68** 041310
[53] Mejía J, Salazar C and Mendoza B S 2005 *Revista Mexicana de Física* **50** 36
[54] Mendoza B, Arzate N, Nastos F and Sipe J 2006 *Phys. Rev.* B **74** 075318
[55] Anderson S M, Mendoza B S and Carriles R 2017 *Phys. Stat. Sol.* B **255** 1700487